Dalton Transactions

PAPER

View Article Online
View Journal | View Issue

Cite this: *Dalton Trans.*, 2017, **46**, 12663

$Li_3Co_{1.06(1)}TeO_6$: synthesis, single-crystal structure and physical properties of a new tellurate compound with Co^{II}/Co^{III} mixed valence and orthogonally oriented Li-ion channels†

Gunter Heymann, *[a] Elisabeth Selb,[a] Michaela Kogler,[b] Thomas Götsch,[b] Eva-Maria Köck,[b] Simon Penner,[b] Martina Tribus[c] and Oliver Janka[d]

A tellurate compound with Co^{II}/Co^{III} mixed valence states and lithium ions within orthogonally oriented channels was realized in $Li_3Co_{1.06(1)}TeO_6$. The single-crystal structure determination revealed two independent and interpenetrating Li/O and (Co,Te)/O substructures with octahedral oxygen coordination of the metal atoms. In contrast to other mixed oxides, a honeycomb-like ordering of CoO_6 and TeO_6 octahedra was not observed. $Li_3Co_{1.06(1)}TeO_6$ crystallizes orthorhombically with the following unit cell parameters and refinement results: *Fddd*, a = 588.6(2), b = 856.7(2), c = 1781.5(4) pm, R_1 = 0.0174, wR_2 = 0.0462, 608 F^2 values, and 33 variables. Additional electron density in tetrahedral voids in combination with neighboring face-linked and under-occupied octahedral lithium sites offers an excellent possible diffusion pathway for lithium ions. According to the symmetry of the crystal structure the diffusion pathways in $Li_3Co_{1.06(1)}TeO_6$ were found in two orthogonal orientations. The Co^{II}/Co^{III} mixed valence was investigated *via* X-ray photoelectron spectroscopy (XPS), revealing a composition comparable to that derived from single-crystal X-ray diffractometry. Magnetic susceptibility measurements underlined the coexistence of Co^{II} and Co^{III}, the title compound, however, showed no magnetic ordering down to low temperatures. The ionic conductivity of $Li_3Co_{1.06(1)}TeO_6$ was determined *via* alternating current (AC) electrochemical impedance spectroscopy and was found to be in the range of 1.6×10^{-6} S cm^{-1} at 573 K.

Received 21st July 2017,
Accepted 25th August 2017

DOI: 10.1039/c7dt02663c

rsc.li/dalton

1 Introduction

Nowadays, there is a great demand for efficient electrical energy storage not only for mobile electric devices but also for regenerative energy resources like solar and wind power. In the case of rechargeable Li-ion batteries, the potentially best chance for improvement lies in the development of new cathode materials. Since 1977, several cathode materials have been used starting with titanium disulphide TiS_2, followed by lithium cobalt dioxide $LiCoO_2$ (1991), lithium manganese spinel $LiMn_2O_4$, and, finally, lithium iron phosphate $LiFePO_4$ (2006).[1] Because of their high stability and easy synthetic accessibility, oxide-based inorganic materials play a major role in the innovation process of electric components.

Hitherto, only little research was carried out in the field of lithium transition metal tellurates as potential cathode materials. This can be attributed to difficulties in the crystallization of these materials and the following crystal structure investigation mostly possible only from powder diffraction data. Recently, a new lithium rich material Li_4NiTeO_6 was synthesized by Sathiya *et al.*, which showed an excellent volume stability and a relatively high capacity of 110 mA h g^{-1}, based on a 2 e$^-$ redox mechanism associated with the Ni^{2+}/Ni^{4+} redox couple.[2] These findings were derived from first-principles investigations on the delithiation process during charging.[3] McCalla *et al.* reported on a material in the lithium rich Li–Fe–Te–O system that exhibited no transition metal oxidation during the charging process. Two oxygen-related mechanisms were identified to contribute to the whole capacity change of $Li_{4.27}Fe_{0.57}TeO_6$ during charge and discharge.[4] The crystal structures of many of these mixed oxides (including various

[a]*Institut für Allgemeine, Anorganische und Theoretische Chemie, Leopold-Franzens-Universität Innsbruck, Innrain 80-82, A-6020 Innsbruck, Austria. E-mail: Gunter.Heymann@uibk.ac.at; Fax: +43(0)512-507 57099*
[b]*Institut für Physikalische Chemie, Leopold-Franzens-Universität Innsbruck, Innrain 52c, A-6020 Innsbruck, Austria*
[c]*Institut für Mineralogie und Petrographie, Leopold-Franzens-Universität Innsbruck, Innrain 52, A-6020 Innsbruck, Austria*
[d]*Institut für Anorganische und Analytische Chemie, Westfälische Wilhelms-Universität Münster, Corrensstraße 28/30, D-48149 Münster, Germany*
†Electronic supplementary information (ESI) available. See DOI: 10.1039/c7dt02663c

superstructure variants) can be attributed to the general formula $A_x(M,L)O_2$ consisting of alkali cations A and brucite-like layers of $(M,L)O_{3/6}$ octahedra. $LiCoO_2$ and its substitution variants with intercalated lithium ions between the octahedral slabs are excellent electrode materials for Li-ion batteries.[5] With sodium instead of lithium, Na_xCoO_2 bronzes are formed, which are efficient thermoelectric materials or even superconductors when hydrated.[6,7] Furthermore, these partially complex oxidic materials show very high alkali-cation conductivity. From tellurates, the compounds $Na_2M_2TeO_6$ (M = Mg, Co, Ni, Zn)[8] and $Na_2LiFeTeO_6$ [9] should be mentioned here exhibiting a pure ionic conductivity of 4–11 S m^{-1} at 573 K. Depending on the different stacking of the brucite-like $(M,L)O_{3/6}$ octahedral layers and in particular on the different coordination of the interlayer alkali cations, various compounds can be classified into different polytypes named O3, P2, P3, *etc.* In this notation, according to Fouassier *et al.*,[10] O stands for octahedral and P for trigonal prismatic coordination of the A ions and the digit for the number of brucite-like layers in the unit cell. In many cases, honeycomb-like superlattice ordering of the two heterovalent M and L cations was observed by the surroundings of isolated LO_6 octahedra from six MO_6 octahedra in a honeycomb-like arrangement. General compositions of these rock-salt type superstructures are $Li_3M^{II}_2LO_6$ (M = Mg, Co, Ni, Cu; L = Nb, Ta, Sb, Bi)[11–17] and $Na_3M^{III}_2LO_6$ (M = Mg, Co, Ni, Cu; L = Sb).[18–20] Compounds belonging to the family of tellurates are $A_2M^{II}_2TeO_6$ (A = Li, Na; M = Mg, Co, Ni, Cu, Zn)[8,21,22] and the recently reported $Li_8M^{II}_2Te_2O_{12}$ (M = Co, Ni, Cu, Zn),[23] which belongs to the former known series $Li_4M^{II}TeO_6$ (M = Ni, Zn).[2,24] An elegant method to obtain isostructural honeycomb-like ordered structures at low temperatures, inaccessible by direct solid state high-temperature reactions, is alkali ion-exchange experiments, as was shown for $Na_2Cu_2TeO_6$.[22] Besides the M^{II}/Te^{VI} honeycomb-like ordering, Tarte *et al.* investigated a possible M^{IV}/Te^{VI} cation ordering and identified two different structure types for the compounds $Li_2(Zr,Hf)TeO_6$ [25] and $Li_2(Ti,Sn)TeO_6$.[26] To the best of our knowledge, in these ordered $A_xM_yTeO_6$ compounds always a heterovalence of M^{II}/Te^{VI} and M^{IV}/Te^{VI} was observed. M^{III} ions occur only in combination with the pentavalent L^V ions, for example in $Li_4M^{III}SbO_6$ (M = Fe)[27] and a possible M^{III}/Te^{VI} ordering is unknown. Within the P2 and O3 family, all the honeycomb-like ordered phases can be attributed to one of the following space groups; the P2 family with known space groups $P6_3/mmc$, $P6_322$, and $P2_12_12_1$ as well as the O3 family with the space groups $C2/m$, $C2/c$, and $P3_12$. Kumar *et al.* reported on a tellurium containing mixed oxide crystallizing in a disordered *Fddd* structure type without a M^{II}/Te^{VI} honeycomb-like ordering.[22] The given unit cell parameters of this compound ($Li_2Ni_2TeO_6$: a = 589.21(7), b = 859.9(1), c = 1769.1(2) pm) are nearly the same as those of the here presented $Li_3Co_{1.06(1)}TeO_6$, also crystallizing without the honeycomb-like ordering in an orthorhombic unit cell with *Fddd* symmetry. Other previously known oxides with an orthorhombic *Fddd* symmetry are $Li_3M^{II}_2LO_6$ (M = Ni, Co, Mg; L = Nb, Ta, Sb)[11–14] with the exception of $Li_3Co_2NbO_6$. As already mentioned, the general observed valences of the M and L ions of the tellurate compounds are M^{II} and M^{IV} in combination with L^{VI}. However, the here presented compound $Li_3Co_{1.06(1)}TeO_6$ is as far as we know the only $A_xM_yTeO_6$ compound exhibiting Co^{III} next to Te^{VI} cations. In contrast to the majority of published structure solutions derived from X-ray powder diffraction data, $Li_3Co_{1.06(1)}TeO_6$ was examined by single-crystal diffraction methods. This method enabled a distinct site assignment and allowed distinguishing between Co^{II}/Co^{III} mixed valence states, which are present in $Li_3Co_{1.06(1)}TeO_6$ or Co^{III}/Li^{I} mixed occupied sites. In order to quantify and differentiate between the Co^{II}/Co^{III} mixed valence states, additional X-ray photoelectron spectroscopy (XPS) as well as magnetic susceptibility measurements were performed. The sample conductivity was determined by two different types of electrochemical impedance experiments.

2 Experimental

2.1 Synthesis

X-ray pure samples with the ideal composition of Li_3CoTeO_6 were synthesized by conventional solid-state techniques. According to eqn (1), mixtures of lithium carbonate (Li_2CO_3: purity ≥99.5%, Fluka), cobalt powder (Co: purity ≥99.8%, Strem Chemicals), and tellurium powder (Te: purity ≥99.99%, Alfa Aesar) in the correct stoichiometric ratio were used.

$$3Li_2CO_3 + 2Co + 2Te + 4.5O_2 \xrightarrow{1173\,K} 2Li_3CoTeO_6 + 3CO_2 \quad (1)$$

The thoroughly ground mixtures of the starting materials were filled into a corundum crucible and placed in an open silica glass ampoule to ensure sufficient oxygen availability. Subsequently, the silica glass ampoules were placed in a vertical tube furnace regulated by using an eight level PID controller with a type K thermocouple. With a heating rate of 1 K min^{-1}, the mixtures were first heated in air to a temperature of 773 K for 3 h to completely oxidize tellurium to its oxidation stage Te^{VI}.[26] Afterwards, the temperature was increased to 1173 K for 36–100 h with a ramp rate of 2 K min^{-1} and then slowly cooled down to a temperature of 473 K with a ramp rate of 0.1 K min^{-1} to ensure good crystal quality. The polycrystalline product appears bluish grey with a metallic lustre and is stable in air. Instead of Li_2CO_3, elemental lithium as a starting material is also possible but more homogeneous results are derived from the syntheses with the carbonate.

2.2 Characterization

Elemental analysis

EDX and ICP. The $Li_3Co_{1.06(1)}TeO_6$ crystals were semi-quantitatively investigated by the use of a Jeol JSM-6010LV scanning electron microscope with a Quantax (Bruker Nano) energy-dispersive system (EDX) for element identification. Small particles of the samples were placed on adhesive carbon platelets and four suitable regions of the crystals were selected as measurement points. The experimentally observed Co to Te ratio in

$Li_3Co_{1.06(1)}TeO_6$ of Co/Te = 21 ± 3 at% Co/17 ± 3 at% Te was close to the ideal ratio of Co/Te = 13.2 at% Co : 12.4 at% Te. The light element Li was not detectable with this measurement setup and the oxygen determination in this semi-quantitative approach is not reliable. Therefore, only the ratios were compared and the absolute values can be neglected.

The Li/Co ratio was determined by ICP-OES (Inductively Coupled Plasma-Optical Emission Spectrometry) on a Horiba Jobin Yvon ACTIVA high-resolution spectrometer. 100.0 ± 0.1 mg of powdered $Li_3Co_{1.06(1)}TeO_6$ sample was completely dissolved in a 50.0 ml nitric acid/hydrogen peroxide mixture (HNO_3 65% p.a. (Carl Roth GmbH), H_2O (ultrapure, 18 MΩ), H_2O_2 30% (Carl Roth GmbH)). The actual measurement solution was diluted twice by a ratio of 1 : 10. Li and Co standard solutions for ICP measurements (Merck) were used to evaluate the concentrations. Calibration curves with a Li and Co content of 0–10–20 mg l^{-1} and 0–40–60 mg l^{-1} were recorded, respectively. The used emission wavelengths were 228.616 nm for Co and 670.784 nm for Li. The given relative standard deviations were calculated on four different measurements. The ICP-OES analysis revealed a content of 439 ± 7 mg l^{-1} Co and 147 ± 4 mg l^{-1} Li within the solution which corresponds to a Li/Co ratio of 2.84(9). This Li/Co ratio was used for the refinement of the site occupancy parameters of the single-crystal structure data.

X-ray diffraction and data collection. For the characterization of the polycrystalline sample of $Li_3Co_{1.06(1)}TeO_6$ by X-ray powder diffraction methods, a STOE Stadi P diffractometer with (111) curved Ge monochromatized Mo-$K_{\alpha1}$ radiation (λ = 70.93 pm) was used. The sample was mounted between two thin acetate films with high-vacuum grease and measured in transmission geometry. The diffraction intensities were collected by using a Dectris MYTHEN2 1K microstrip detector with 1280 strips. The lattice parameters derived from the Rietveld refinements agree well with those obtained from the single-crystal data (see Table 1). Details about the Rietveld refinement as well as the Rietveld plot (Fig. S1†) are given in the ESI.†

A couple of crystal fragments of the crushed sample were embedded in polyfluoropolyalkylether (viscosity 1800) and treated under a microscope. Smaller fragments of $Li_3Co_{1.06(1)}TeO_6$ appear transparent blue. Selected single-crystal fragments were fixed on the tip of MicroMounts™ (MiTeGen, LLC, Ithaca, NY, USA) with a diameter of 30 μm and a subsequent intensity data collection of the $Li_3Co_{1.06(1)}TeO_6$ crystals was carried out using a Bruker D8 Quest diffractometer with a Photon 100 detector system and an Incoatec Microfocus source generator (multi-layered optic, monochromatized Mo-K_α radiation, λ = 71.073 pm). To enhance the collection strategies concerning ω- and φ-scans, the APEX 2 program package[28] was used and data sets of complete reciprocal spheres up to high angles with high redundancies were received. Further data processing and data reduction were performed with the program SAINT[28] and a correction regarding absorption effects was carried out on the semi-empirical "multi scan" approach with the program SADABS.[28]

Table 1 Crystal data and structure refinement of $Li_3Co_{1.06(1)}TeO_6$ (standard deviations in parentheses)

Empirical formula	$Li_3Co_{1.06(1)}TeO_6$
Molar mass, g mol^{-1}	307.03
Crystal system	Orthorhombic
Space group	*Fddd* (no. 70)
Formula units per cell, *Z*	8
Powder diffractometer	STOE Stadi P
Radiation	Mo-$K_{\alpha1}$ (λ = 70.93 pm)
Powder data:	
a, pm	587.81(1)
b, pm	857.71(2)
c, pm	1787.72(3)
V, Å^3	896.78(3)
Single-crystal diffractometer	Bruker D8 Quest
Radiation	Mo-K_α (λ = 71.073 pm)
Single-crystal data:	
a, pm	588.6(2)
b, pm	856.7(2)
c, pm	1781.5(4)
V, Å^3	898.4(3)
Calculated density, g cm^{-3}	4.54
Crystal size, mm^3	0.04 × 0.03 × 0.03
Temperature, K	273(2)
Absorption coefficient, mm^{-1}	10.3
F (000), e	1102
Detector distance, mm	40
θ range, °	4.4–37.9
Range in *hkl*	±10, ±14, ±30
Total reflections	11 929
Data/ref. parameters	608/33
Reflections with $I \geq 2\sigma(I)$	535
R_{int}, R_σ	0.0316, 0.0112
Goodness-of-fit on F^2	1.378
Absorption correction	Multi-scan[28]
R_1/wR_2 for $I \geq 2\sigma(I)$	0.0174/0.0462
R_1/wR_2 (all data)	0.0216/0.0477
Largest diff. peak/hole, e Å^{-3}	1.89/−0.75
Extinction coefficient	0.0012(2)
Transmission min./max.	0.695/0.747

Physical property measurements

Magnetic properties. The powdered sample of $Li_3Co_{1.06(1)}TeO_6$ was packed into polyethylene (PE) capsules and attached to the sample holder rod of a Vibrating Sample Magnetometer (VSM) unit for measuring the magnetization $M(T,H)$ in a Quantum Design Physical Property Measurement System (PPMS). The samples were investigated in the temperature range of 2.5–300 K with magnetic flux densities up to 80 kOe.

X-ray photoelectron spectroscopy (XPS). The oxidation states of the samples were investigated by X-ray photoelectron spectroscopy (XPS) using a Thermo Scientific MultiLab 2000 spectrometer. This instrument is equipped with a monochromated Al-K_α X-ray source, an Alpha 110 hemispherical sector analyzer as well as an ion gun for sputter-depth profiling (with 3 keV argon ions), and features a base pressure in the low 10^{-10} mbar range. In order to avoid charging of the samples upon irradiation, a flood gun, providing electrons of 6 eV, was utilized.

The Li 1s, Te 3d and C 1s spectra were fitted using Gaussian/Lorentzian products (30% Lorentzian character). Because of the complex shape of the Co 2p region, reference spectra had to be employed to determine the amount of Co^{III}

in the samples. Due to the lack of a pure oxidic Co^{III} reference, references from CoO and Co_3O_4 were used. To determine the Co^{III} concentration, a linear combination of the respective sample spectrum and the CoO reference was fitted to the Co_3O_4 spectrum, which allows for the determination of Co^{III} amounts larger than that in Co_3O_4. During the sputter depth profiling, using adventitious carbon as the charge reference was not possible (because it was sputtered away during the first step). The latter was used for the surface spectra, and the other spectra were referenced to the Co 2p region because no peak shift between Co^{II} and Co^{III} was observed.[29]

Electrochemical impedance spectroscopy (EIS). The *in situ* impedance cell consists of an outer quartz tube with two inner quartz tubes to which the sample and the electrodes were attached. Heating is provided by using a tubular Linn furnace and controlled by the use of a thermocouple (K-element) located in the reactor about 5 mm downstream of the sample and a Micromega PID temperature controller.[30] The impedance is measured by using an IM6e impedance spectrometer (Zahner Messsysteme, Germany), which provides data on the impedance and the phase angle of the current as a function of voltage. The powder samples were pressed into pellets with a pressure of 1.5 t (5 mm diameter, 0.1 mm thick) and placed between two circular Pt electrodes forming a plate capacitor in mechanically enforced contact with the sample pellet.

For all temperature-programmed impedance measurements, 20 mV signal amplitude and a frequency of 1 Hz were applied to the Pt electrodes. The impedance modulus value $|Z|$ of the pellet was, thus, effectively measured in an electrochemically unpolarized state.

The electrical properties were also determined by AC EIS measurements in a frequency range between 100 mHz and 1 MHz with 20 mV signal amplitude. The real and imaginary parts of the impedance were first measured from 1 kHz up to 1 MHz (within 19 s) and then from 1 MHz down to 100 mHz (within 4 min 37.7 s; total measuring time: 4 min 56.7 s) to check for changes of the system during EIS. A 1 h interval was allowed for thermal stabilization after each temperature change. Curve fitting and resistance calculation were performed with the Zahner ThalesBox and with an adapted equivalent circuit model consisting of two R-CPE elements in series as described in ref. 31 and 32.

3 Results and discussion

3.1 Structure refinements

The diffraction data showed an F-centered orthorhombic lattice and the systematic extinctions were in agreement with the space group *Fddd*. The starting atomic parameters were derived from the "Intrinsic Phasing" method,[33] implemented in the APEX 2 program package.[28] Subsequently, full-matrix least squares refinements based on F^2 were executed with the program SHELXL-2013.[34,35] All atoms were refined with anisotropic displacement parameters. The correct composition of the compound was verified by refining the occupation parameters in a separate series of least-squares cycles. Except the Co and Li atoms, all sites were fully occupied within two standard deviations. The ideal composition of Li_3CoTeO_6 with all Co atoms in the oxidation state Co^{III} is formed by one fully occupied tellurium site (8*a*), two oxygen sites (16*f*, 32*h*) as well as two lithium sites (8*b*, 16*g*). The Co site (16*g*) is only half filled resulting in the following refinement residuals: R_1 = 0.0190/wR_2 = 0.0526, and GooF = 1.340. A possible ordering of Co on the 16*g* site was checked by symmetry reduction to the space group *Fdd*2. The two resulting 8*a* sites were more than 50% occupied without the ordering tendency and the Flack parameter of around 0.5 indicated centro-symmetry. Separate refinements of the occupation of Co and Li sites in the centrosymmetric space group *Fddd* revealed significant deviations from the ideal composition Li_3CoTeO_6. Cobalt exhibits a site occupation of 52.7% and the Li2 site seems to be occupied only by 73.6%, leading to a composition of $Li_{2.6(1)}Co_{1.06(1)}TeO_6$ and slightly improved refinement results of: R_1 = 0.0172/wR_2 = 0.0460, and GooF = 1.372. The Li1 site is completely occupied within two standard deviations. In addition to this, residual electron density in a tetrahedral oxygen environment was left and taking into account this by an occupation with lithium and free refinement of the occupation parameters, the general Li site becomes occupied by 12(2)%. The resulting composition of $Li_{2.97(9)}Co_{1.05(1)}TeO_6$ is in good agreement with the EDX, ICP, and XPS measurements. Unfortunately, lithium located at this tetrahedral position face-linked to the octahedral position is defined as non-positive (NPD). For this reason, the occupation parameters of Li2 were raised manually to achieve the former given composition $Li_{2.97(9)}Co_{1.05(1)}TeO_6$ (Li/Co = 2.83) reflecting the measured Li/Co ratio of 2.84 derived from the ICP measurement. The composition $Li_3Co_{1.06(1)}TeO_6$ (Li/Co = 2.83) was achieved by a full occupation of the Li2 site. This increased the thermal anisotropic displacement parameters of Li2. Actually, however, a part of the Li2 atoms will be statistically distributed to the neighboring tetrahedral positions. Possible Li/Co mixed occupations were considered in various refinement cycles but did not improve the structure model nor reflected the results of the additional analyses. Nevertheless, mixed occupations in this highly dynamic system cannot be excluded or are even most likely. The correctness of the space group was checked with the ADDSYM[36] routine of the PLATON program package.[37] Detailed information about the single-crystal structure determination can be found in Table 1. The positional parameters, anisotropic displacement parameters, interatomic distances, and angles are given in Tables 2–5.

Further details of the structure refinements may be obtained from the Fachinformationszentrum Karlsruhe, D-76344 Eggenstein-Leopoldshafen, Germany (fax: (+49)7247-808-666; e-mail: crysdata@fiz-karlsruhe.de), on quoting the deposition number CSD 433117 ($Li_3Co_{1.06(1)}TeO_6$).

3.2 Crystal chemistry

The here presented compound $Li_3Co_{1.06(1)}TeO_6$ crystallizes orthorhombically with the following unit cell parameters and

Table 2 Atomic coordinates, occupation, and isotropic equivalent displacement parameters U_{eq} [Å^2] for $Li_3Co_{1.06(1)}TeO_6$ (space group: *Fddd*). U_{eq} is defined as one third of the trace of the orthogonalized U_{ij} tensor (standard deviations in parentheses)

Atom	Wyckoff-position	x	y	z	SOF	U_{eq}
Co	16*g*	3/8	3/8	0.04298(4)	0.532(2)	0.0075(3)
Te	8*a*	1/8	1/8	1/8	1	0.00457(8)
O1	16*f*	1/8	0.3499(3)	1/8	1	0.0086(4)
O2	32*h*	0.1076(3)	0.3742(2)	0.29817(8)	1	0.0087(3)
Li1	8*b*	3/8	3/8	3/8	1	0.017(2)
Li2	16*g*	3/8	3/8	0.2135(8)	1	0.05(4)

Table 3 Anisotropic displacement parameters [Å^2] for $Li_3Co_{1.06(1)}TeO_6$, (space group: *Fddd*) (standard deviations in parentheses)

Atom	U_{11}	U_{22}	U_{33}	U_{23}	U_{13}	U_{12}
Co	0.0079(4)	0.0077(4)	0.0068(3)	0	0	−0.0029(3)
Te	0.0043(1)	0.0050(1)	0.0044(1)	0	0	0
O1	0.0088(8)	0.0060(7)	0.0111(8)	0	0.0013(8)	0
O2	0.0076(6)	0.0109(6)	0.0076(5)	−0.0003(5)	0.0019(4)	0.0008(6)
Li1	0.008(4)	0.032(5)	0.010(4)	0	0	0
Li2	0.054(8)	0.045(7)	0.041(6)	0	0	0.038(6)

Table 4 Selected interatomic distances (pm) of $Li_3Co_{1.06(1)}TeO_6$ (standard deviations in parentheses)

Co:	O1	208.50(6)	2×
	O2	212.4(2)	2×
	O2	213.9(2)	2×
Te:	O1	192.6(2)	2×
	O2	193.6(2)	4×
Li1:	O2	208.6(2)	4×
	O1	235.7(2)	2×
Li2:	O2	216.1(2)	2×
	O1	216.8(9)	2×
	O2	218.0(9)	2×

Table 5 Selected interatomic angles (°) of $Li_3Co_{1.06(1)}TeO_6$ (standard deviations in parentheses)

O2–Co–O2	80.29(9)	
O1–Co–O2	80.38(8)	2×
O2–Co–O2	89.94(6)	2×
O1–Co–O1	91.01(3)	
O2–Co–O2	93.85(6)	2×
O1–Co–O2	94.61(4)	2×
O1–Co–O2	96.11(7)	2×
O1–Co–O2	172.36(6)	2×
O2–Co–O2	175.05(9)	
O1–Te–O2	89.79(5)	4×
O2–Te–O2	89.98(9)	2×
O2–Te–O2	90.02(9)	2×
O1–Te–O2	90.21(5)	4×
O2–Te–O2	179.58(9)	2×
O1–Te–O1	180	
O2–Li1–O2	82.03(9)	2×
O2–Li1–O1	89.80(4)	4×
O2–Li1–O1	90.20(4)	4×
O2–Li1–O2	97.97(9)	2×
O2–Li1–O2	179.61(9)	2×
O1–Li1–O1	180	
O2–Li2–O1	78.4(2)	2×
O1–Li2–O1	86.6(5)	
O1–Li2–O2	90.73(5)	2×
O2–Li2–O2	91.7(2)	2×
O2–Li2–O2	92.4(5)	
O2–Li2–O1	93.5(3)	2×
O2–Li2–O2	96.0(2)	2×
O2–Li2–O2	169.0(7)	
O1–Li2–O1	173.6(2)	2×

refinement results: *Fddd*, a = 588.6(2), b = 856.7(2), c = 1781.5(4) pm, R_1 = 0.0174, wR_2 = 0.0462, 608 F^2 values and 33 variables. The unit cell parameters are close to the isopointal compound $Li_2Ni_2TeO_6$ reported by Kumar *et al.* but because of the low thermal stability, they did not attempt to grow single crystals. From powder data they derived a disordered structure type without a Ni^{II}/Te^{VI} honeycomb-like ordering and Li^{I}/Ni^{II} mixed occupation of the 8*b* and the two 16*g* sites.[22] Our single-crystal investigations confirmed the missing honeycomb-like ordering and furthermore, $Li_3Co_{1.06(1)}TeO_6$ exhibits a comparatively high-order three-dimensional lattice of two interpenetrating substructures. These two substructures consist of a lithium–oxygen and a cobalt/tellurium–oxygen structure part. During various refinement cycles, mixed occupations of the cobalt and lithium sites were tested. A simultaneous refinement of both Li sites together with the Co site as Li/Co mixed occupied sites according to Kumar *et al.*[22] was not possible. In addition to this, refinements of the under-occupied Co site as the mixed Li/Co site resulted in a compound with a Li/Co ratio larger than that detected by the ICP measurements. Moreover, the additional Li site remains non-positive definite (NPD) and for a valence balanced compound a combination of Co^{III} and Co^{IV} would be necessary. This is in conflict with the results of the XPS measurements which specify the Co^{II}/Co^{III} ratio to 9(3)% Co^{II} and 91(3)% Co^{III}. For the Co site, an occupation of 53(1)% was found after a free refinement of the occupation parameters. The diffraction data gave no hints of a symmetry reduction and an ordering of the Co site in a larger unit cell. Due to the fact that the Co site is a Co^{II}/Co^{III} mixed valent site, the occupation must be larger than 50% compared to the ideal formula sum of Li_3CoTeO_6 with 100% Co^{III}. For this reason, a statistical occupation of the Co site is assumed. The structural model proposed here is the most suitable model with the joint consideration of all here presented analytical results.

Fig. 1 gives an impression of the crystal structure of $Li_3Co_{1.06(1)}TeO_6$ along the [110] direction (bottom) and of the 90° turned view along the [$\bar{1}$10] direction (top). Both sights reveal an identical linking pattern of edge linked TeO_6 and CoO_6 octahedra. However, it should be noted that the displayed Co octahedra are only about 53% occupied in a statistical manner. This part of the crystal structure belongs to the first substructure of the two interpenetrating networks. Within the so-formed channels, the lithium ions are located building up the second substructure if drawn in their polyhedral view. Fig. 2 shows the crystal structure of $Li_3Co_{1.06(1)}TeO_6$ with the

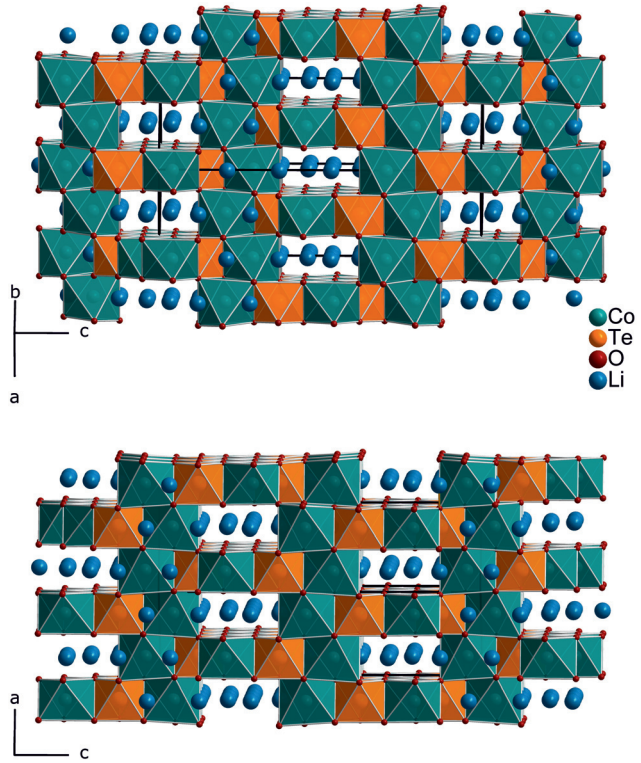

Fig. 1 The crystal structure of $Li_3Co_{1.06(1)}TeO_6$ with a view along the [1̄10] direction (top) and the 90° turned (rotation around the *c*-axis) view along the [110] direction (bottom). TeO_6 and CoO_6 octahedra are drawn in orange and petrol, respectively. The lithium atoms are located inside the channels of the crystal structure.

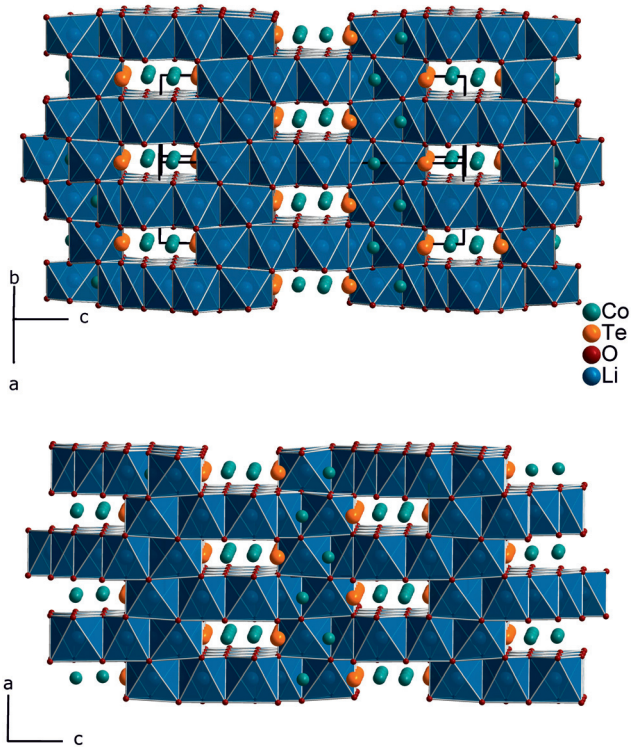

Fig. 2 Inverted crystal structure of $Li_3Co_{1.06(1)}TeO_6$ with emphasized LiO_6 polyhedra and Co and Te located inside the channels. Viewing direction [1̄10] (top) and the 90° turned (rotation around the *c*-axis) view along the direction [110] (bottom).

only displayed LiO_6 octahedra network in identical directions as before. Now the Co and Te atoms are located inside the channels. Each atom in this structure type exhibits an octahedral coordination sphere like it is found in rock-salt type structures. The Te atoms are coordinated in nearly perfect octahedral geometry with typical Te^{VI}–O distances of 193 (2×) and 194 pm (4×) and O–Te–O angles of 89.8–90.2° (see Tables 4 and 5). The octahedral Co coordination sphere is a bit more distorted with Co–O distances from 209–214 pm and O–Co–O angles varying from 80.3 to 96.2° which are comparable to Co^{II}–O distances of 213 pm found in NaCl-type CoO.[38] Spinel-type Co_2O_3 with tetrahedral and octahedral Co coordination exhibits Co^{II}–O (tetrahedral position) and Co^{III}–O (octahedral position) distances of 198 and 189 pm, respectively.[39] Cobalt in its threefold low-spin oxidation state can be found in corundum type high-pressure sesquioxide with Co–O distances of 189 and 193 pm.[40] Compared to binary cobalt oxide polymorphs, the Co–O contacts appearing in $Li_3Co_{1.06(1)}TeO_6$ are comparatively long for Co^{III}–O distances. However, in ternary or quaternary Co-containing compounds for example $LiCoO_2$,[41] $CoLa_2Li_{0.5}Co_{0.5}O_4$,[42] and $Ba_6La_2Co_4O_{15}$[43] Co^{III}–O distances in an octahedral configuration from 205 to 215 pm are documented. The Li1 atoms show four equal distances of 209 pm to the surrounding oxygen atoms and two longer contacts of 236 pm. A more uniform coordination is given for the Li2 atoms, which are encircled by six oxygen atoms with distances of 216–218 pm. All corresponding angles of the octahedral coordination spheres can be found in Table 5. In the literature, the documented range of Li–O distances in lithium-transition metal-tellurates is around 200 pm but can be escalated up to 247 pm and more. In $Li_8Cu_2Te_2O_{12}$, a coordination comparable to the Li1 atoms occurs with four shorter Li–O distances of 201 pm and two longer distances of 247 pm.[23] The anisotropic displacement parameters of the lithium ions inside the octahedral coordination sphere are enlarged, indicating a possible Li ion mobility. As described in the Structure refinement section, the Li1 site is fully occupied within two standard deviations, whereas the Li2 site revealed an under-occupation and was filled up manually until the Li/Co ratio determined by ICP analyses was achieved. This was also legitimated by the fact that additional electron density located in a neighboring tetrahedral position resulted in the same Li/Co ratio if taken into account. However, an occupation of this tetrahedral position with lithium resulted in negative displacement parameters. Nevertheless, the located electron density in a tetrahedral environment in combination with direct face-linked under-occupied octahedral sites offers an excellent diffusion pathway for lithium ions. According to the crystal structure, two of these diffusion pathways in the orthogonal orientation exist in $Li_3Co_{1.06(1)}TeO_6$. In Fig. 3 the diffusion pathway along the [110] direction with Li–Li hopping distances

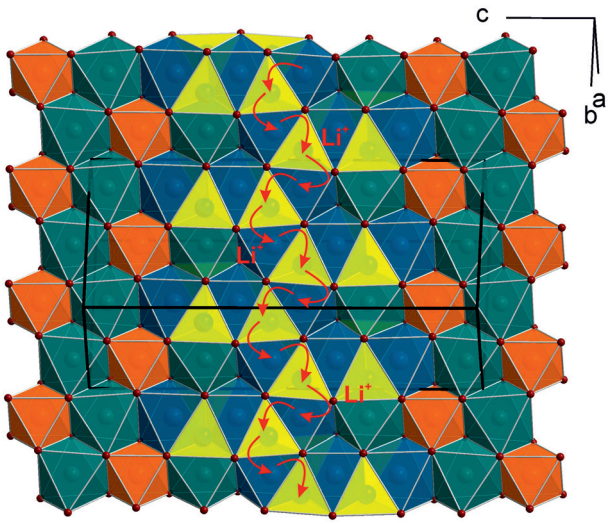

Fig. 3 Possible diffusion pathway from octahedral to tetrahedral sites for Li-ions within one octahedral slab. The diffusion pathways run along the [110] direction and a second identical pathway direction is parallel to the [$\bar{1}$10] direction.

of 179–186 pm is emphasized. The second diffusion pathway runs along the [$\bar{1}$10] direction. Investigations of the physical properties of $Li_3Co_{1.06(1)}TeO_6$ are discussed in the following section.

3.3 Physical properties

Magnetic properties. Magnetic susceptibility measurements were conducted in a zero-field-cooled (ZFC) mode between 3 and 300 K at an external field strength of 10 kOe. The data were corrected by the diamagnetic contributions of the PE capsule and the diamagnetic contributions of the constituent ions of $\chi(Li_3CoTeO_6) = -97 \times 10^{-6}$ emu mol^{-1} ($\chi(Li^+) = -1 \times 10^{-6}$ emu mol^{-1}; $\chi(Co^{3+}) = -10 \times 10^{-6}$ emu mol^{-1}; $\chi(Te^{6+}) = -12 \times 10^{-6}$ emu mol^{-1} and $\chi(O^{2-}) = -12 \times 10^{-6}$ emu mol^{-1}).[44] The χ and χ^{-1} data are depicted in Fig. 4 (top). No magnetic ordering phenomena are visible down to low temperatures. From the inverse susceptibility, the effective magnetic moment is calculated to be $\mu_{eff} = 4.32(1)\mu_B$. This magnetic moment is higher than the expected moment for Co^{2+} (d^7, high-spin) of $3.88\mu_B$ but also lower compared to the calculated moment of $4.90\mu_B$ for a Co^{3+} cation (d^6, high-spin). Taking the Co^{II}/Co^{III} ratio of 1 : 9 determined by XPS into account, the expected magnetic moment for $Li_3Co_{1.06(1)}TeO_6$ is $4.81\mu_B$, considering all Co cations in the high-spin state. When considering Co^{2+} to be in a low-spin state ($\mu_{calc} = 1.73\mu_B$), the total effective magnetic moment adds up to $4.68\mu_B$. Co^{3+} as the low-spin cation has an effective moment of $0\mu_B$; therefore, this case cannot apply. Both cases result in magnetic moments that are higher than the experimentally found value of $\mu_{eff} = 4.32(1)\mu_B$; therefore, more detailed information about the magnetic spin-state of the Co cations cannot be given. The experimentally determined value, however, points towards high-spin Co^{3+} and low-spin Co^{2+}.

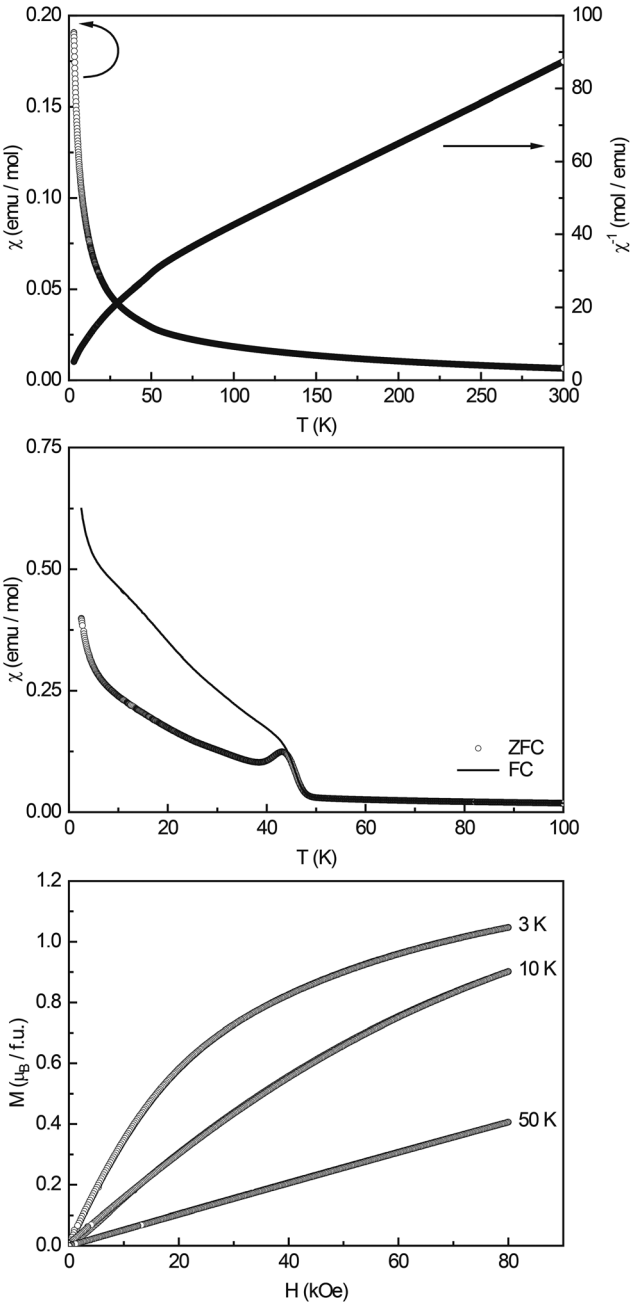

Fig. 4 Magnetic properties of $Li_3Co_{1.06(1)}TeO_6$: susceptibility and inverse susceptibility (χ and χ^{-1} data), measured at an external field strength of 10 kOe (top); zero-field-cooled/field-cooled data (ZFC/FC) measured at 100 Oe (middle); magnetization isotherms recorded at 3, 10, and 50 K (bottom).

Low-field measurements between 2.5 and 100 K (Fig. 4, middle) show an antiferromagnetic transition at $T_N = 43.5(2)$ K; the Curie-tail towards low temperatures and the magnitude of the transition however indicate that the AFM ordering is not intrinsic. In the literature, several ternary cobalt tellurates and lithium cobalt oxides are found which exhibit magnetic ordering. $CoTe_6O_{13}$ has a Néel temperature of $T_N = 21$ K[45] and $Co_2Te_3O_8$ of $T_N = 70$ K.[46] Co_3TeO_6 was found to exhibit a

complex magnetism with transitions T_1 = 26 K, T_2 = 19.5 K, and T_3 = 18 K,[47] $LiCo_2O_4$ orders antiferromagnetically at $T_N \sim$ 35 K,[48] and the solid solution $Li_{1-x}Co_xO$ at temperatures >200 K.[49] Li_6CoO_4 [50] and $Li_8Co_2Te_2O_6$ [23] finally only show paramagnetic behavior and no magnetic ordering down to low temperatures. Therefore, no clear indication of the origin of the magnetic ordering at ~40 K can be found, substitutional effects as *e.g.* seen in $Li_{1-x}Co_xO$ show that the ordering temperature shifts towards lower temperatures upon increasing Li content. Hence, one could speculate that Li-substituted $Co_2Te_3O_8$ could cause the observed transition.

The magnetization isotherms recorded at 3, 10, and 50 K (Fig. 4, bottom) finally show the typical behavior of a paramagnetic material, with slightly curved isotherms at 3 and 10 K. The saturation magnetization at 3 K and 80 kOe was determined to be $\mu_{sat} = 1.05(1)\mu_B$.

X-ray photoelectron spectroscopy. The results of an XPS sputter depth profile are shown in Fig. 5. In (a), the Li 1s region is highlighted, revealing that there is no Li visible at the surface (bottom-most spectrum). It has to be noted that the Li 1s core level has an extremely low sensitivity factor of about 0.057 as compared to *e.g.* 19.2 for the Co 2p region.[51] Thus, the same amount of lithium results in a peak that is more than 330 times smaller than that of cobalt. Hence, the possibility exists that low amounts of lithium were indeed present, but were hidden within the noise in the spectrum. Upon short sputtering to a depth of 5 nm, a distinct feature emerged consisting of two peaks. In fact, it was possible to fit the signal by a combination of two peaks of the same width that were 1.85 eV apart. These two states were assigned to the two octahedrally coordinated lithium sites. A correlation of associated binding energies and lithium sites was difficult. Most likely, the state with higher binding energy (54.45 eV) was due to Li1 exhibiting four short (209 pm) and two long (236 pm) Li–O contacts, whereas the second one (52.6 eV) originated from the Li2 site, which featured six Li–O contacts between 216 and 218 pm. The latter made up 28% of the total Li seen in that spectrum (18(7) at% of all elements observed, see also Table 6). As described above, the Li2 site revealed a site occupation of only 74% by free refinement of the site occupation parameters. During the structure refinement, the site occupation was manually increased with respect to the measured Li/Co ratio from ICP, and due to the observed electron density at a neighboring tetrahedral position. This variability of the Li2 occupation was also observed *via* XPS. At a depth of 25 nm, the Li signal became even more prominent, still being comprised of

Table 6 Quantification obtained from the XPS depth profile

	at%			
Etch depth/nm	Li	Co	Te	O
0	0	26(2)	11.0(6)	63(5)
5	18(7)	30.0(7)	10.6(2)	42(2)
25	23(9)	26.2(13)	13.4(3)	38(4)
75	39(4)	17.7(6)	13.3(2)	30(2)

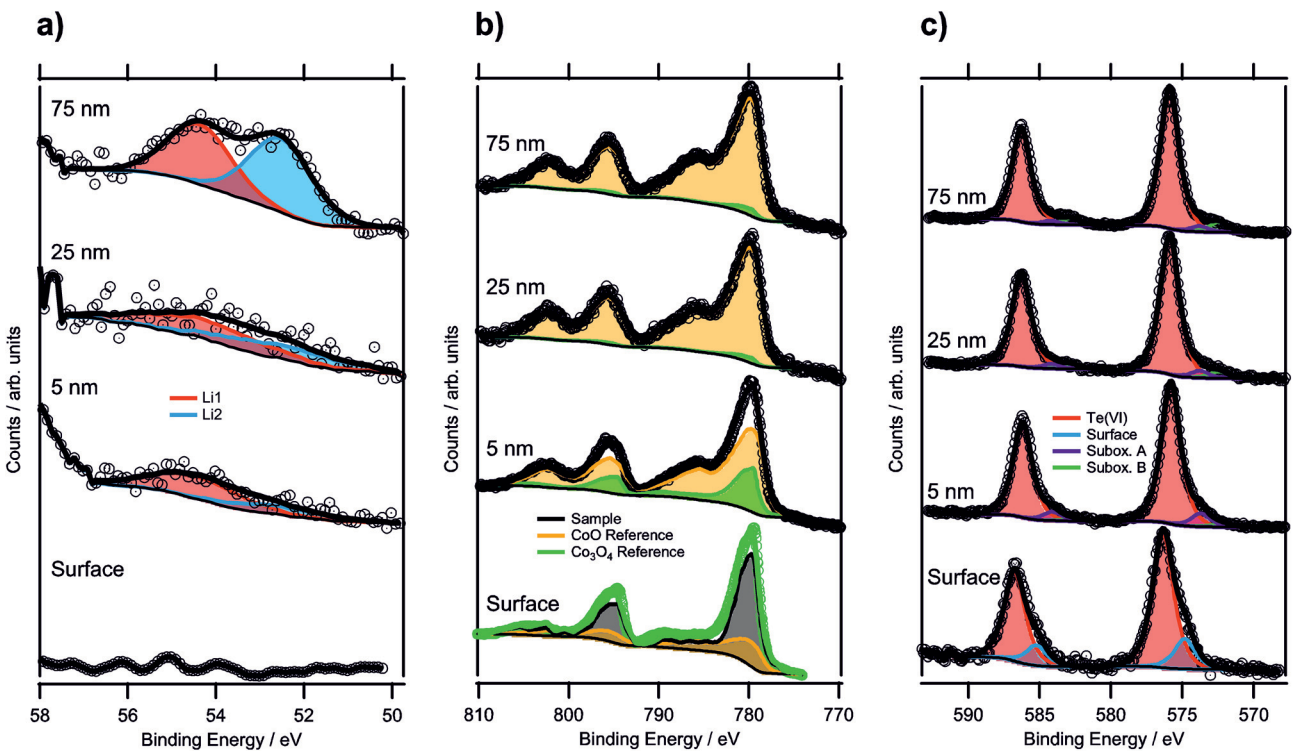

Fig. 5 XPS depth profile spectra of a sample annealed for 100 h (up to a maximum depth of 75 nm): (a) Li 1s regions, (b) Co 2p regions and (c) Te 3d regions of the same depth profiling experiment.

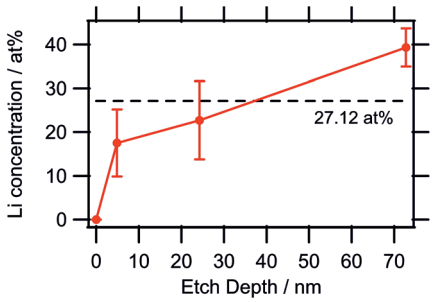

Fig. 6 Lithium concentration depth profile as determined by XPS. The large error bars are due to the very low sensitivity factor of Li causing the noise to have a higher impact on the quantification.

the same two compounds as described above (at 54.35 and 52.5 eV, respectively). The fraction of occupied Li2 sites had increased to 45%. After further sputtering until a depth of 75 nm was reached, the Li 1s signal intensity was significantly larger. Moreover, the Li1/Li2 ratio changed to 45 : 55, *i.e.* the sampled depth of approximately 2.8 nm for the kinetic energy of the Li 1s electrons[52] contained slightly more of the Li2 species (again located at a binding energy of 52.5 eV). The Li content seemed to be highly variable within the bulk sample depending on the ratio of Co^{II}/Co^{III} valences. This can also be gathered from the results of the quantification, listed in Table 6, as well as from the lithium concentration profile in Fig. 6, with the dashed line representing the expected Li concentration based on the sum formula (27.12 at%). Whereas at 5 nm, the amount of Li was lower than that value, it was within the standard deviation at 25 nm, and at 75 nm, the observed Li concentration was actually significantly higher than the expected value, which corroborated this theory.

In Fig. 5b, the Co 2p regions are displayed for each depth profiling step. In order to determine the oxidation state of the cobalt in the structure, the reference spectra of CoO and Co_3O_4 were used. However, the surface spectrum (bottom-most spectrum) could not be fitted by a linear combination of these two references due to the higher Co^{III} concentration as compared to Co_3O_4, and no reliable pure Co^{III} reference could be obtained. Therefore, a different fitting procedure had to be applied for this surface spectrum. Instead of using the sample spectrum as the one to be fitted, the Co_3O_4 spectrum was used. The Co_3O_4 reference was, thus, fitted by a linear combination of the CoO spectrum and the sample spectrum. The fitting equation is shown by the following formula, with S_x being the spectra of compound x and I_x the respective intensity factors:

$$S_{Co_3O_4} = I_{CoO} \times S_{CoO} + I_{sample} \times S_{sample}$$

Since the amount of Co^{III} is the quantity of interest, and CoO contains only Co^{II}, all the Co^{III} required for the description of Co_3O_4 (corresponding to 66.67%) has to come from the sample compound. Thus, the intensity of the sample spectrum can directly be linked to the concentration of Co^{III} in the sample by rewriting this equation to $c(Co^{III}, Co_3O_4) = 2/3 = I_{sample} \times c(Co^{III}, sample)$, with $c(Co^{III}, x)$ describing the Co^{III} concentration of compound x. Since the fitting procedure showed that the Co_3O_4 spectrum can be described by a linear combination of 27% of the CoO spectrum and 73% of the sample spectrum, the Co^{III} concentration in the sample was 91(3)%. This means that the average oxidation state of cobalt in the oxide was 2.91(9). From the formula sum, the calculated theoretical oxidation state was 2.83, assuming that tellurium was only present as Te^{VI}, which was within the experimental errors of this analysis.

The surface oxidation state of a sample, annealed for 36 hours only, was analyzed too, and showed 89(3)% of Co^{III}, which is in excellent agreement with the sample annealed for 100 h. This indicated that the oxidation of Co had already been completed after 36 hours heat treatment.

Upon sputtering the specimen annealed for 100 hours, the oxidation state of Co was reduced significantly, shown in the top three spectra in Fig. 5b. For these spectra, the fitting of a linear combination of CoO and Co_3O_4 was possible, because the Co^{III} concentration was lower than that for Co_3O_4. At 5 nm, the sum of 75% CoO and 25% Co_3O_4 described the spectrum well, resulting in a Co^{III} concentration of 16.8% in the sample corresponding to an oxidation state of 2.17. This drastic shift in the oxidation state can also be seen from the satellite feature to the high binding energy side of the $2p_{3/2}$ component, which was shifted to lower binding energies with increasing Co^{II} concentration. At 25 nm, the Co ions were reduced even further, leading to only 2% of Co^{III} and a sum oxidation state of 2.02. Upon reaching a depth of 75 nm, no change compared to the 25 nm depth was detected. This strong reduction of the cobalt species most likely resulted from the sputtering process itself by bombardment with highly energetic argon ions (such as the 3 keV ones employed here). It is known that especially transition metals are affected to be reduced by preferential sputtering with argon ions.[53,54]

The Te 3d components featured a distinct shoulder at the lower binding energy sides (see Fig. 5c). While the majority of the signal could be described by a component with a binding energy of 576.4 eV for $3d_{5/2}$, and thus could be attributed to Te^{VI},[55] the asymmetry of the peaks required a second component at 574.8 eV to be added. Based on the binding energy, this could originate from a Te^{IV} species,[56] which was expected to exist on the surface exhibiting a lower coordination number for tellurium. Similar surface species are known for various other compounds such as Sr-rich perovskites or yttrium oxide.[57,58] Because Te^{IV} accounted for 18% of the total Te 3d signal with an escape depth of 2.02 nm of the corresponding electrons, an overlayer thickness of 0.37 nm could be assumed relating to a single atomic layer. This gives strong evidence that Te^{IV} is a surface species. The presence of Te^{IV} also indicated that the crystal is tellurium-terminated, instead of being, *e.g.* cobalt-terminated. For confirmation, ion scattering data giving information about the outermost surface composition would be required.

During sputtering, there was a noticeable peak shift in the Te 3d region, as the major component was at a binding energy

of 575.8 eV. In the literature, there are reports of mixed $Te^{IV/VI}$ oxides resulting in peaks in this area.[56] However, it was still located 1.0 eV higher than the possible Te^{IV} species, attributed to the surface spectrum. The difference in binding energy further confirmed the assignment of Te^{IV} as a surface species. Additionally, small contributions from suboxidic species with binding energies of 573.7 eV and 572.4 eV were identified. The lower binding energy component could even be attributed to elemental Te,[55,59] but exact assignment was difficult with a low concentration making up only 2% of the total spectrum. Further sputtering steps did not alter the spectrum significantly.

AC electrochemical impedance spectroscopy analysis. The sample conductivity was determined by two different types of electrochemical impedance experiments: (i) frequency-dependent measurements and (ii) time-/temperature-dependent impedance measurements (ii) (details are given in the ESI†).

Frequency-dependent impedance measurements (Nyquist plots). To gain information on the ionic conductivity of the sample, frequency dependent EIS measurements (Nyquist plots) were performed for $Li_3Co_{1.06(1)}TeO_6$. The tests were conducted in air between RT and 723 K. The $Li_3Co_{1.06(1)}TeO_6$ sample shows the characteristic semicircles as displayed in Fig. 7 indicating the ionic conductivity of the material. At temperatures between 523 and 573 K, two depressed semicircles are apparent: a very large one at high frequencies and a small one at low frequencies. The bulk (b) contribution is usually observed at high frequencies in the Nyquist plot, whereas the grain boundary (gb) contribution is located at mid and low frequencies.[30,60–62] The equivalent circuit model that was used in this study to fit the experimental data is composed of constant phase elements (CPEs) instead of ideal Debye's capacitors. This is generally done for polycrystalline samples due to material inhomogeneity, surface defects, ionic transport deviation from Fick's law, and electrode roughness. All these parameters give rise to a certain degree of frequency dispersion and non-uniformity of the current density. Hence, a CPE represents more accurately the capacitive behavior of this kind of cell in the whole studied frequency range.[30,63–65] This can also be clearly seen in the depressed semicircles in Fig. 7. It is shown that with an increase in temperature, R_b and R_{gb} decrease. The determined b and gb resistances were then converted to electrical conductivities (σ) by considering the thickness (0.1 mm) and area (0.196 cm^2) of the sample (see Table 7).

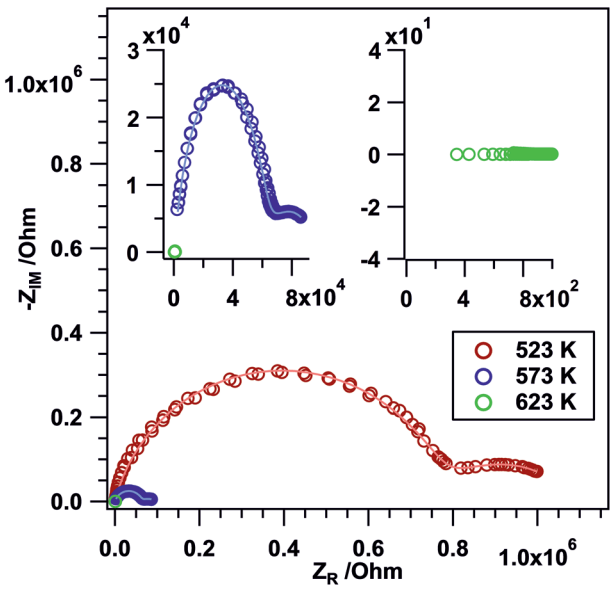

Fig. 7 AC impedance spectra (data points) and simulated spectra (continuous lines) of the bulk and grain boundary contribution of the $Li_3Co_{1.06(1)}TeO_6$ sample in air at selected temperatures between 523 and 623 K. The lowest frequency of 0.1 Hz is at the right side and the highest one of 1 MHz at the left side of the *x*-axis. The insets show zoomed regions of the Nyquist plots (NPs) at higher temperatures.

Kumar *et al.* determined the ionic conductivities for the compound $Li_2Ni_2TeO_6$ which crystallizes isopointal to our investigated sample $Li_3Co_{1.06(1)}TeO_6$ and reported values in the range of 2×10^{-4} S cm^{-1} at 573 K. This value is about two orders of magnitude higher than the grain boundary conductivity σ_{gb} of 1.64×10^{-6} S cm^{-1} measured for $Li_3Co_{1.06(1)}TeO_6$ at 523 K. The differences in conductivity may be explained by changes in the lattice polarization (Ni^{II} instead of Co^{III}), changes in the lithium coordination geometries (significant occupation of tetrahedral voids) and site occupation. Comparable values were found for the lithium-containing garnets $Li_3Ln_3Te_2O_{12}$ (Ln = Y, Pr, Nd, Sm–Lu) with a maximum value of 1×10^{-5} S cm^{-1} at 873 K measured for the neodymium compound.[66] In crystalline solids, the highest reported Li^+ conductivities of about 1×10^{-3} S cm^{-1} at room temperature have been realized in a perovskite-type lithium lanthanum titanate.[67,68]

However, starting at a temperature of 623 K and above only a straight line in the corresponding NPs is visible. The imaginary part of the impedance is basically zero and only a "real" resistance (without a phase shift) is observed indicating a significantly increased conductivity with ohmic resistance contributions.

Time-/temperature-dependent impedance measurements. Time- and temperature dependent AC impedance experiments were carried out to check for eventual phase transformations in the studied temperature region. At first, the same temperature region as used for the NPs was chosen. At RT, an impedance

Table 7 Circuit parameters used to model the AC impedance spectra in Fig. 7

Temperature/K	R_b/Ω	σ_b/S cm^{-1}	C_b/F	R_{gb}/Ω	σ_{gb}/S cm^{-1}	C_{gb}/F
523	6.82×10^5	7.47×10^{-8}	3.56×10^{-11}	1.87×10^5	2.72×10^{-8}	6.17×10^{-8}
573	8.07×10^4	6.31×10^{-7}	3.06×10^{-11}	3.10×10^4	1.64×10^{-6}	4.88×10^{-9}

value of 2.26×10^7 Ω is apparent. Upon heating to ~353 K the impedance starts to increase leading to a value of 8.27×10^9 Ω. In the temperature region between 353 and 723 K, semiconductive behavior with a decreasing impedance value upon increasing the temperature is visible. Basically, the same impedance course is visible upon re-cooling to RT with slight differences between 371 K and RT. No directly visible phase transformation processes are apparent during the heating–cooling cycle. Further details as well as plots of the time- and temperature-dependent *in situ* EIS measurements (Fig. S2†) are given in the ESI.†

4 Conclusion

The compound $Li_3Co_{1.06(1)}TeO_6$ synthesized under high-temperature conditions exhibited Li-ion conductivity as well as Co^{II}/Co^{III} mixed valence states. In contrast to the isopointal compound $Li_2Ni_2TeO_6$ reported by Kumar *et al.*, the here presented $Li_3Co_{1.06(1)}TeO_6$ revealed M^{III} ions next to Te^{VI} ions for the first time. Magnetic susceptibility measurements and XPS investigations clearly indicated the presence of Co^{III} in this compound, although the exact quantification is difficult. ICP measurements were supposed to be the most accurate way to quantify the Li and Co content of a 100 mg $Li_3Co_{1.06(1)}TeO_6$ sample. The Li/Co ratio thus obtained was used for the single-crystal structure refinement and resulted in completely occupied Li sites after consideration of additional electron density in tetrahedral voids. Consequently, for reasons of electroneutrality, the cobalt site must be mixed valent, which was proved by magnetic susceptibility and XPS measurements. The facts that XPS measurements even indicated a higher lithium content in the sample, and the effective magnetic moment proposed a lower Co^{III} content than 91(3)% suggest that $Li_3Co_{1.06(1)}TeO_6$ could be a promising electrode material based on the Co^{II}/Co^{III} redox couple.

Conflicts of interest

There are no conflicts to declare.

Acknowledgements

We would like to thank Prof. Dr. H. Huppertz for continuous support and usage of all the facilities of the Institute of General, Inorganic and Theoretical Chemistry, University of Innsbruck. For the execution of the ICP measurements we thank Ass. Prof. Dr. R. Tessadri, Institute of Mineralogy and Petrography. This work was financially supported by the *Tiroler Wissenschaftsfond* (TWF); project no.: 235863. Dr. G. Heymann was supported by the program *Nachwuchsförderung* of the University Innsbruck. T. Götsch acknowledges funding by the Austrian Science Fund (FWF) *via* grant F4503-N16. This work was performed within the framework of the research platform "Material's and Nanoscience" at the University of Innsbruck.

References

1 M. S. Whittingham, *MRS Bull.*, 2008, **33**, 411–419.
2 M. Sathiya, K. Ramesha, G. Rousse, D. Foix, D. Gonbeau, K. Guruprakash, A. S. Prakash, M. L. Doublet and J. M. Tarascon, *Chem. Commun.*, 2013, **49**, 11376–11378.
3 J. Bao, D. Wu, Q. Tang, Z. Ma and Z. Zhou, *Phys. Chem. Chem. Phys.*, 2014, **16**, 16145–16149.
4 E. McCalla, A. S. Prakash, E. Berg, M. Saubanère, A. M. Abakumov, D. Foix, B. Klobes, M.-T. Sougrati, G. Rousse, F. Lepoivre, S. Mariyappan, M.-L. Doublet, D. Gonbeau, P. Novak, G. Van Tendeloo, R. P. Hermann and J.-M. Tarascon, *J. Electrochem. Soc.*, 2015, **162**, A1341–A1351.
5 J. B. Goodenough and Y. Kim, *Chem. Mater.*, 2010, **22**, 587–603.
6 I. Terasaki, Y. Sasago and K. Uchinokura, *Phys. Rev. B: Condens. Matter*, 1997, **56**, R12685–R12687.
7 K. Takada, H. Sakurai, E. Takayama-Muromachi, F. Izumi, R. A. Dilanian and T. Sasaki, *Nature*, 2003, **422**, 53–55.
8 M. A. Evstigneeva, V. B. Nalbandyan, A. A. Petrenko, B. S. Medvedev and A. A. Kataev, *Chem. Mater.*, 2011, **23**, 1174–1181.
9 V. B. Nalbandyan, A. A. Petrenko and M. A. Evstigneeva, *Solid State Ionics*, 2013, **233**, 7–11.
10 C. Fouassier, C. Delmas and P. Hagenmuller, *Mater. Res. Bull.*, 1975, **10**, 443–449.
11 M. Castellanos, J. A. Gard and A. R. West, *J. Appl. Crystallogr.*, 1982, **15**, 116–119.
12 J. G. Fletcher, G. C. Mather, A. R. West, M. Castellanos and M. P. Gutierrez, *J. Mater. Chem.*, 1994, **4**, 1303–1305.
13 G. C. Mather, R. I. Smith, J. M. S. Skakle, J. G. Fletcher, M. A. Castellanos R, M. P. Gutierrez and A. R. West, *J. Mater. Chem.*, 1995, **5**, 1177–1182.
14 G. C. Mather and A. R. West, *J. Solid State Chem.*, 1996, **124**, 214–219.
15 J. M. S. Skakle, M. A. Castellanos R, S. T. Tovar and A. R. West, *J. Solid State Chem.*, 1997, **131**, 115–120.
16 E. A. Zvereva, M. A. Evstigneeva, V. B. Nalbandyan, O. A. Savelieva, S. A. Ibragimov, O. S. Volkova, L. I. Medvedeva, A. N. Vasiliev, R. Klingeler and B. Buechner, *Dalton Trans.*, 2012, **41**, 572–580.
17 R. Berthelot, W. Schmidt, S. Muir, J. Eilertsen, L. Etienne, A. W. Sleight and M. A. Subramanian, *Inorg. Chem.*, 2012, **51**, 5377–5385.
18 O. A. Smirnova, V. B. Nalbandyan, A. A. Petrenko and M. Avdeev, *J. Solid State Chem.*, 2005, **178**, 1165–1170.
19 V. V. Politaev, V. B. Nalbandyan, A. A. Petrenko, I. L. Shukaev, V. A. Volotchaev and B. S. Medvedev, *J. Solid State Chem.*, 2010, **183**, 684–691.
20 L. Viciu, Q. Huang, E. Morosan, H. W. Zandbergen, N. I. Greenbaum, T. McQueen and R. J. Cava, *J. Solid State Chem.*, 2007, **180**, 1060–1067.
21 J. Xu, A. Assoud, N. Soheilnia, S. Derakhshan, H. L. Cuthbert, J. E. Greedan, M. H. Whangbo and H. Kleinke, *Inorg. Chem.*, 2005, **44**, 5042–5046.

22 V. Kumar, A. Gupta and S. Uma, *Dalton Trans.*, 2013, **42**, 14992–14998.
23 V. Kumar, N. Bhardwaj, N. Tomar, V. Thakral and S. Uma, *Inorg. Chem.*, 2012, **51**, 10471–10473.
24 V. B. Nalbandyan, M. Avdeev and M. A. Evstigneeva, *J. Solid State Chem.*, 2013, **199**, 62–65.
25 J. Choisnet, A. Rulmont and P. Tarte, *J. Solid State Chem.*, 1988, **75**, 124–135.
26 J. Choisnet, A. Rulmont and P. Tarte, *J. Solid State Chem.*, 1989, **82**, 272–278.
27 E. A. Zvereva, O. A. Savelieva, Y. D. Titov, M. A. Evstigneeva, V. B. Nalbandyan, C. N. Kao, J. Y. Lin, I. A. Presniakov, A. V. Sobolev, S. A. Ibragimov, M. Abdel-Hafiez, Y. Krupskaya, C. Jahne, G. Tan, R. Klingeler, B. Buchner and A. N. Vasiliev, *Dalton Trans.*, 2013, **42**, 1550–1566.
28 *APEX2 (v. 2014.11-0), CELL_NOW (v. 2008/4), SAINT (v. 8.34A), TWINABS (v. 2012/1), and SADABS (v. 2014/5)*, Bruker AXS GmbH, Karlsruhe, Germany.
29 Thermo Scientific XPS Reference, Thermo Fisher Scientific Inc., http://www.xpssimplified.com, (accessed 23.05.2017, 2017).
30 M. Kogler, E. M. Köck, B. Klötzer, L. Perfler and S. Penner, *J. Phys. Chem. C*, 2016, **120**, 3882–3898.
31 H. J. Avila-Paredes, J. Zhao, S. Wang, M. Pietrowski, R. A. De Souza, A. Reinholdt, Z. A. Munir, M. Martin and S. Kim, *J. Mater. Chem.*, 2010, **20**, 990–994.
32 N. J. Kidner, N. H. Perry, T. O. Mason and E. J. Garboczi, *J. Am. Ceram. Soc.*, 2008, **91**, 1733–1746.
33 G. Sheldrick, *Acta Crystallogr., Sect. A: Fundam. Crystallogr.*, 2015, **71**, 3–8.
34 G. M. Sheldrick, *ShelXL – Crystal Structure Refinement – Multi-CPU Version*, University of Göttingen.
35 G. Sheldrick, *Acta Crystallogr., Sect. C: Cryst. Struct. Commun.*, 2015, **71**, 3–8.
36 Y. Le Page, *J. Appl. Crystallogr.*, 1988, **21**, 983–984.
37 A. Spek, *Acta Crystallogr., Sect. D: Biol. Crystallogr.*, 2009, **65**, 148–155.
38 P. Schmidt, *Eur. J. Inorg. Chem.*, 2008, 2847–2855, DOI: 10.1002/ejic.200800218.
39 W. L. Smith and A. D. Hobson, *Acta Crystallogr., Sect. B: Struct. Crystallogr. Cryst. Chem.*, 1973, **29**, 362–363.
40 J. Chenavas, J. C. Joubert and M. Marezio, *Solid State Commun.*, 1971, **9**, 1057–1060.
41 H. J. Orman and P. J. Wiseman, *Acta Crystallogr., Sect. C: Cryst. Struct. Commun.*, 1984, **40**, 12–14.
42 S. Abou-Warda, W. Pietzuch, G. Berghöfer, U. Kesper, W. Massa and D. Reinen, *J. Solid State Chem.*, 1998, **138**, 18–31.
43 H. Mevs and H. Müller-Buschbaum, *Z. Anorg. Allg. Chem.*, 1990, **584**, 114–118.
44 G. A. Bain and J. F. Berry, *J. Chem. Educ.*, 2008, **85**, 532.
45 J. T. S. Irvine, M. G. Johnston and W. T. A. Harrison, *Dalton Trans.*, 2003, 2641–2645, DOI: 10.1039/B300573A.
46 C. R. Feger, G. L. Schimek and J. W. Kolis, *J. Solid State Chem.*, 1999, **143**, 246–253.
47 C.-W. Wang, C.-H. Lee, C.-Y. Li, C.-M. Wu, W.-H. Li, C.-C. Chou, H.-D. Yang, J. W. Lynn, Q. Huang, A. B. Harris and H. Berger, *Phys. Rev. B: Condens. Matter*, 2013, **88**, 184427.
48 O. Peña, V. Bodenez, T. Guizouarn, E. Meza and J. L. Gautier, *J. Magn. Magn. Mater.*, 2004, **272–276**(Supplement), E1579–E1580.
49 W. D. Johnston, R. R. Heikes and D. Sestrich, *J. Phys. Chem. Solids*, 1958, **7**, 1–13.
50 A. Möller, *Chem. Mater.*, 1998, **10**, 3196–3201.
51 *CasaXPS: Processing Software for XPS, AES, SIMS and More*, Casa Software Ltd.
52 W. H. Gries, *Surf. Interface Anal.*, 1996, **24**, 38–50.
53 T. Götsch, W. Wallisch, M. Stöger-Pollach, B. Klötzer and S. Penner, *AIP Adv.*, 2016, **6**, 025119.
54 T. Götsch, T. Schachinger, M. Stöger-Pollach, R. Kaindl and S. Penner, *Appl. Surf. Sci.*, 2017, **402**, 1–11.
55 W. E. Sartz, K. J. Wynne and D. M. Hercules, *Anal. Chem.*, 1971, **43**, 1884–1887.
56 B. V. R. Chowdari and P. Pramoda Kumari, *J. Non-Cryst. Solids*, 1996, **197**, 31–40.
57 R. Thalinger, T. Götsch, C. Zhuo, W. Hetaba, W. Wallisch, M. Stöger-Pollach, D. Schmidmair, B. Klötzer and S. Penner, *ChemCatChem*, 2016, **8**, 2057–2067.
58 E.-M. Köck, M. Kogler, T. Götsch, B. Klötzer and S. Penner, *Phys. Chem. Chem. Phys.*, 2016, **18**, 14333–14349.
59 J. M. Thomas, I. Adams, R. H. Williams and M. Barber, *J. Chem. Soc., Faraday Trans. 2*, 1972, **68**, 755–764.
60 L. Rojo, G. Ga Mandayo and E. Castano, Thin film YSZ solid state electrolyte characterization performed by electrochemical impedance spectroscopy, 9th Spanish Conference on Electron Devices (CDE), Valladolid, Spain, 2013.
61 M. Wierzbicka, P. Pasierb and M. Rekas, *Physica B*, 2007, **387**, 302–312.
62 E. M. Köck, M. Kogler, B. Klötzer, M. F. Noisternig and S. Penner, *ACS Appl. Mater. Interfaces*, 2016, **8**, 16428–16443.
63 K. Obal, Z. Pedzich, T. Brylewski and M. Rekas, *Int. J. Electrochem. Sci.*, 2012, **7**, 6831–6845.
64 S. Vishweswaraiah, Masters Thesis, Central Florida, 2004.
65 J. R. MacDonald, *Impedance Spectroscopy - Theory, Experiment and Applications*, Wiley, New York, 1987.
66 M. P. O'Callaghan, D. R. Lynham, E. J. Cussen and G. Z. Chen, *Chem. Mater.*, 2006, **18**, 4681–4689.
67 S. Stramare, V. Thangadurai and W. Weppner, *Chem. Mater.*, 2003, **15**, 3974–3990.
68 A. D. Robertson, A. R. West and A. G. Ritchie, *Solid State Ionics*, 1997, **104**, 1–11.